Contra-Rotating Open Rotor Tone Noise Prediction

Edmane Envia[1]
NASA Glenn Research Center, Cleveland, OH 44135

Reliable prediction of contra-rotating open rotor (CROR) noise is an essential element of any strategy for the development of low-noise open rotor propulsion systems that can meet both the community noise regulations and cabin noise limits. Since CROR noise spectra exhibit a preponderance of tones, significant efforts have been directed towards predicting their tone content. To that end, there has been an ongoing effort at NASA to assess various in-house open rotor tone noise prediction tools using a benchmark CROR blade set for which significant aerodynamic and acoustic data have been acquired in wind tunnel tests. In the work presented here, the focus is on the nearfield noise of the benchmark open rotor blade set at the cruise condition. Using an analytical CROR tone noise model with input from high-fidelity aerodynamic simulations, tone noise spectra have been predicted and compared with the experimental data. Comparisons indicate that the theoretical predictions are in good agreement with the data, especially for the dominant tones and for the overall sound pressure level of tones. The results also indicate that, whereas the individual rotor tones are well predicted by the combination of the thickness and loading sources, for the interaction tones it is essential that the quadrupole source is also included in the analysis.

Nomenclature

c_0	=	ambient speed of sound
e_j	=	unit vector component in the radiation direction
f_i	=	blade force per unit area
g_c	=	acoustic convective phase factor
M_{0_R}	=	medium Mach number in the radiation direction
n_j	=	surface unit normal vector
$p'(\mathbf{x},t)$	=	acoustic pressure
$\hat{p}_k(\mathbf{x})$	=	Fourier harmonic of aerodynamic loading on the blade
$p'_{\mathcal{T}_m}(\mathbf{x})$	=	Fourier harmonic of thickness tone noise
$p'_{\mathcal{L}_{m,k}}(\mathbf{x})$	=	Fourier harmonic of loading tone noise
$p'_{\mathcal{Q}_{m,k}}(\mathbf{x})$	=	Fourier harmonic of quadrupole tone noise
R	=	distance between source and observer (radiation distance)
S_{B_1}	=	blade surface
T_{ij}, $\hat{T}_{ij_k}$	=	Lighthill stress tensor and its Fourier harmonic component
U_{0_j}	=	medium ambient velocity components
V_{B_1}	=	volume surrounding the blade
v_n	=	normal component of blade surface velocity

---

[1] Research Aerospace Engineer, Acoustics Branch, M.S. 54-3, 21000 Brookpark Road, Associate Fellow.

$\mathbf{x}$, x_i	=	observer Cartesian coordinates in stationary frame of reference
$\mathbf{y}$, y_j	=	source Cartesian coordinates in stationary frame of reference
$\tilde{\mathbf{y}}$	=	source Cartesian coordinates in rotating frame of reference
κ	=	convective amplitude factor
ρ_0	=	ambient air density
φ, φ_s	=	observer and source azimuthal coordinates

I. Introduction

In recent years, due to the rising cost of aviation fuel, there has been renewed interest in contra-rotating open rotor (CROR) propulsion technology in both the U.S. and Europe. Changes in the design paradigm and the advent of three-dimensional aerodynamic design tools have enabled CROR designs that can meet aggressive fuel burn targets as well as community noise limits. In contrast to the vintage 1980s designs, modern CROR designs (see Figure 1) have unequal blade counts, larger rotor-rotor spacings and diameters, and lower rotational speeds. These features enable modern designs to retain their inherent fuel efficiency advantage over turbofans and, at the same time, meet current community noise regulations with margin to spare. Of course, in addition to the community noise limits, a successful open rotor design must also meet cabin noise limits to be viable commercially.

Figure 1. On the left GE36-UDF propfan demonstrator engine installed on the MD-81 test bed aircraft in 1987 is shown. On the right is a model of a modern contra-rotating open rotor engine design from Snecma. Whereas the front and aft rotor blade counts were same on the UDF demonstrator engine (8 x 8), the modern CROR engine designs feature unequal blade counts (typically, 12 x 10).

Designing low-noise CROR propulsion systems that can meet community noise standards and are also compatible with passenger comfort requires noise prediction tools that are both accurate and robust. Since CROR engines produce an abundance of tone noise, there has been much emphasis on ensuring that their tone noise spectra can be reliably predicted.

To address this challenge, a NASA research effort has been focused on assessing current open rotor tone noise prediction tools and on identifying the potential areas of improvement. To that end, a commercial aerodynamic simulation tool is being used in conjunction with NASA open rotor noise codes to predict the noise characteristics of a benchmark CROR blade set over a wide range of operating conditions encompassing both the takeoff/landing and climb/cruise conditions. The resulting predictions are systematically assessed against extensive aerodynamic and acoustic databases that have been acquired for this benchmark blade set. The focus of this paper is on providing an assessment of the prediction capability for the nearfield noise of the benchmark open rotor blade set at the cruise condition. The nearfield noise at cruise has implications for cabin noise.

The CROR blade set used in this study is a relatively modern GE design called F31/A31 whose front and aft rotor blade counts are 12 and 10, respectively. Extensive low-speed and high-speed aerodynamic and acoustic data have been acquired in the NASA wind tunnels for a model scale version of this blade set. The model scale blade set features composite blades with a front rotor diameter of 0.66 m (25.8 inches) and an aft rotor diameter of 0.63 m (24.9 inches). The rotor-rotor spacing for all the cases discussed in this paper was set at 0.2 m (7.8 inches). The high-speed tests were conducted in the NASA 8-foot x 6-foot (i.e., 2.4 m x 1.8 m) wind tunnel to investigate the aero/acoustic performance at the cruise condition.[1] Aerodynamic and acoustic data used for comparisons in this paper were acquired for F31/A31 in un-installed configuration (i.e., no fuselage simulator or pylon) and at zero angle of attack. This data is a subset of a much larger database of configurations that were tested in the wind tunnel.

II. Aeroacoustic Modeling

The existing approaches for open rotor tone noise prediction run the gamut of fidelity from the empirical ones on the one end to the fully numerical methods on the other. However, the bulk of existing capability lies in the middle ground where the difficulties associated with the large scale-disparity between the nonlinear aerodynamic field and

the linear acoustic field are addressed by "separating" the two fields. A common way for doing this is to use Lighthill's acoustic analogy approach or, rather, its extension developed by Ffowcs-Williams and Hawkings.[2] The resulting expression of the acoustic analogy, often referred to as the Ffowcs-Williams and Hawkings (FW-H) equation, describes the acoustic field as temporal and spatial ensembles over the aerodynamic source regions of interest (i.e., rotor blade surfaces S and the volume surrounding the blades V). Following Goldstein's notation, the FW-H equation can be written as[3]

$$p'(\mathbf{x},t) = \underbrace{\int_{-\infty}^{\infty}\int_{S(\tau)} \rho_0 v_n \frac{D_0 G}{D\tau}\, dS(\mathbf{y})d\tau}_{\text{Thickness Noise}} + \underbrace{\int_{-\infty}^{\infty}\int_{S(\tau)} f_i \frac{\partial G}{\partial y_i}\, dS(\mathbf{y})d\tau}_{\text{Loading Noise}} + \underbrace{\int_{-\infty}^{\infty}\int_{V(\tau)} T_{ij} \frac{\partial^2 G}{\partial y_i \partial y_j}\, d\mathbf{y}\, d\tau}_{\text{Quadrupole Noise}}$$ (1)

$$f_i = -(p - p_0)n_i, \quad T_{ij} = \rho u_i u_j + \delta_{ij}\left[(p - p_0) - c_0^2(\rho - \rho_0)\right]$$

where the aerodynamic source terms f_i and T_{ij} are, in general, time-dependent. Only the inviscid parts of these terms are considered here because their viscous parts do not play an important role in CROR tone noise generation. For moving surfaces (i.e., rotor blades), both S and V are also time-dependent in the stationary frame of reference. The three terms on the right hand side represent the contributions of the thickness, loading, and quadrupole sources to the acoustic field. The aerodynamic sources must be measured or computed before Eq. (1) can be explicitly evaluated. Most often this is done using Unsteady Reynolds Averaged Navier-Stokes (URANS) models. The approach used in this paper for predicting CROR tone noise is based on an asymptotic approximation to the FW-H equation in conjunction with a commercial CFD code used for computing the necessary aerodynamic input. The moving medium Green's function in Eq. (1) is given by

$$G(\tau) = \frac{1}{4\pi\kappa R}\delta\left(t - \tau - g_c R/c_0\right)$$

$$g_c(\tau) = \frac{1}{\beta_0^2}\left(\kappa - M_{0_R}\right), \quad \kappa(\tau) = \sqrt{M_{0_R}^2 + \beta_0^2}, \quad M_{0_R}(\tau) = M_{0_i} e_i$$ (2)

$$e_i(\tau) = \frac{(x_i - y_i)}{R}, \quad R(\tau) = |\mathbf{x}(\tau) - \mathbf{y}(\tau)|, \quad \beta_{0_i} = \sqrt{1 - M_{0_i}^2}, \quad M_{0_i} = \frac{U_{0_i}}{c_0}$$

Once the geometry of the rotors, their loading distribution, and the quadrupole source distribution in the vicinity of the rotors are specified, Eq. (1) can be explicitly evaluated to estimate the acoustic field generated by the open rotor for a given observer. This can be done by carrying out the indicated spatial and temporal integrals numerically in the time domain (e.g., see Farassat[4]). However, often the FW-H equation is tackled in the frequency domain and by assuming that the observer is in the farfield. This assumption results in considerable simplification of the integrands and leads to analytic expressions for the integrals over the source time τ. The spatial integrations are then carried out using a quadrature scheme to calculate the acoustic farfield. Hanson's CROR noise model[5] is an example of such an approach. Parry[6] took Hanson's approach further by using a large-blade-count asymptotic approximation to the blade surface integrals to derive explicit analytic expressions for the acoustic field thus obviating the need for calculating the spatial integrals. This approximation relies on simplifying assumptions about the blade geometry, which could limit the utility of the model for highly three-dimensional blades currently being considered. In addition, neither of these CROR noise models dealt explicitly with the quadrupole source contribution primarily because the earlier studies of rotating blade noise had indicated that the quadrupole source becomes significant for transonic and supersonic tip relative Mach numbers only (e.g., Ffowcs Williams and Hawkings[7]).

For the work described in this paper, an alternative approach has been used to evaluate the FW-H equation that eliminates the need for the farfield assumption or the blade geometry approximation. The end result is an accurate analytic approximation to the FW-H equation that is valid everywhere in the acoustic field and retains the geometric complexity of the blade. In addition, this model also accounts for the quadrupole source explicitly. This alternative approach is described in detail in the papers by Envia[8,9] and will be briefly outlined here.

A. Acoustic Formulas

Let the blade counts of the two rotors be denoted by B_1 & B_2 and their rotational speeds by N_1 & N_2 where the subscript "1" and "2" refer to the front and aft rotors, respectively. It should be noted that the open rotor blade counts and their rotational speeds need not, and frequently are not, equal. Let the rotational axis of the two rotors be aligned with the x-axis of a right-handed coordinate system as shown in Figure 2. Assume that the front rotor is rotating clockwise (looking downstream) and the aft rotor is rotating counter-clockwise. Further, assume that the forward flight direction (or, equivalently, the direction of the principal flow convection) is aligned with the x-axis and is in the positive x-direction.

Owing to the linearity of acoustic field, Eq. (1) can be evaluated for each rotor separately and the results combined to give the acoustic field associated with the CROR. It should be noted that even though these contributions are computed separately, the aerodynamic coupling of the two rotors is explicitly taken into account in the analysis. As shown in Ref. 9, the tonal acoustic field generated by the front rotor of the CROR has the following form,

Figure 2. Sketch of F31/A31 contra-rotating open rotor geometry and coordinate system. The stacking axis of the aft rotor is located at $x = 0.0$ m and that of the front rotor is located at $x = -0.2$ m (-7.84 inches).

$$p'(\mathbf{x},t) = \sum_{m=-\infty}^{\infty}{}' p'_{T_m}(\mathbf{x}) e^{-imB_1\Omega_1 \, t} + \sum_{m=-\infty}^{\infty}{}' \sum_{k=-\infty}^{\infty} \left[p'_{\mathcal{L}_{m,k}}(\mathbf{x}) + p'_{Q_{m,k}}(\mathbf{x}) \right] e^{-i(mB_1\Omega_1 + kB_2\Omega_2) \, t} \qquad (3)$$

where p'_{T_m}, $p'_{\mathcal{L}_{m,k}}$ and $p'_{Q_{m,k}}$ denote the harmonic amplitudes of the thickness, loading and quadrupole noise sources, respectively, and $\Omega_1 = 2\pi N_1$ & $\Omega_2 = 2\pi N_2$ denote the rotational frequencies of the two rotors. Note that, whereas the thickness noise is produced at the multiples of the front rotor blade passing frequency $mB_1\Omega_1 = mBPF_1$, the loading noise and quadrupole noise are produced at the combination frequencies $mB_1\Omega_1 + kB_2\Omega_2 = mBPF_1 + kBPF_2$ as a result of the aerodynamic coupling between the two rotors.[*] The indices m and k designate acoustic and unsteady flow harmonics, respectively. The prime on the summation over the index m implies that the term $m = 0$ does not contribute to the sound field.

Deriving explicit expressions for the harmonic amplitudes in Eq. (3) requires the use of the FW-H equation and that, in turn, necessitates accurate evaluation of the associated spatial and temporal integrals for realistic rotor geometries, operating conditions, and flowfields. The analyses described in Refs. 8 and 9 show how a large-blade-count asymptotic approximation[†] can be successfully applied to the integrations over the source time τ to derive explicit analytic expressions for these integrals without the use of the farfield approximation employed by Hanson.[5] In addition, since the resulting expressions are uniformly valid across the subsonic/supersonic tip speed divide, they obviate the need for the patching required in Parry's asymptotic approximation (see Crighton and Parry[10]) to get a uniformly valid description from the subsonic to the supersonic tip speed regimes. Another benefit of the approximation described in Refs. 8 and 9 is that it allows the retention of the geometric complexity of the rotor blades and their associated aerodynamic flowfield in order to model highly complex configurations. Since, the description of the asymptotic analysis is rather involved, the details will not be repeated here. Instead, only the final working expressions for the various harmonic amplitudes will be given. For the front rotor these are
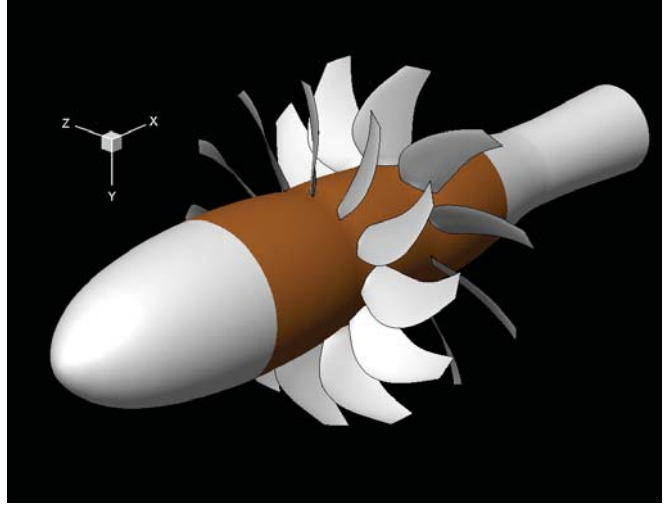
---

[*] The blade passing harmonic tones (i.e., $nBPF_1$ and $nBPF_2$) are determined by the mean flowfield. The interaction tones (i.e., $mBPF_1 + kBPF_2$ for $k \neq 0$) are determined by the harmonics of the unsteady flowfield.

[†] The approximation is formally valid for $B_1 \gg 1$, but, in practice, it is remarkably accurate for $B_1 > 2$.

$$p'_{T_m}(\mathbf{x}) \simeq iB_1 \sum_{n=1}^{2} \int_{S_{B_1}} \frac{\mathcal{A}_{T_m}^{(n)}}{R^n} e^{mB_1(\mu-i\Psi)} \left\{ d_{0,n} \frac{Ai\left[\left(mB_1\right)^{2/3}\gamma^2\right]}{\left(mB_1\right)^{1/3}} + d_{1,n} \frac{Ai'\left[\left(mB_1\right)^{2/3}\gamma^2\right]}{\left(mB_1\right)^{2/3}} \right\}_T dS(\tilde{\mathbf{y}})$$

$$\Psi = \frac{1}{\beta_{0_1}} M_{\text{tip}_1} M_{0_1} \chi_s + \varphi_s - \varphi$$

(4a)

$$p'_{\mathcal{L}_{m,k}}(\mathbf{x}) \simeq iB_1 \sum_{n=1}^{2} \int_{S_{B_1}} \frac{\mathcal{A}_{\mathcal{L}_{m,k}}^{(n)}}{R^n} e^{(mB_1-kB_2)(\mu-i\Psi)} \left\{ d_{0,n} \frac{Ai\left[\left(mB_1-kB_2\right)^{2/3}\gamma^2\right]}{\left(mB_1-kB_2\right)^{1/3}} + d_{1,n} \frac{Ai'\left[\left(mB_1-kB_2\right)^{2/3}\gamma^2\right]}{\left(mB_1-kB_2\right)^{2/3}} \right\}_{\mathcal{L}} dS(\tilde{\mathbf{y}})$$

If $mB_1 - kB_2 \neq 0 \rightarrow \Psi = \frac{1}{\beta_{0_1}}\eta_{\text{CRF}} M_{\text{tip}_1} M_{0_1}\chi_s + (\varphi_s - \varphi), \qquad \eta_{\text{CRF}} = \frac{mB_1 + kB_2\Omega_2/\Omega_1}{mB_1 - kB_2}$

(4b)

If $mB_1 - kB_2 = 0 \rightarrow \Psi = \frac{1}{\beta_{0_1}}\eta_{\text{CRF}} M_{\text{tip}_1} M_{0_1}\chi_s, \qquad \eta_{\text{CRF}} = 1 + \frac{\Omega_2}{\Omega_1}$

$$p'_{\mathcal{Q}_{m,k}}(\mathbf{x}) \simeq iB_1 \sum_{n=1}^{3} \int_{V_{B_1}} \frac{\mathcal{A}_{\mathcal{Q}_{m,k}}^{(n)}}{R^n} e^{(mB_1-kB_2)(\mu-i\Psi)} \left\{ d_{0,n} \frac{Ai\left[\left(mB_1-kB_2\right)^{2/3}\gamma^2\right]}{\left(mB_1-kB_2\right)^{1/3}} + d_{1,n} \frac{Ai'\left[\left(mB_1-kB_2\right)^{2/3}\gamma^2\right]}{\left(mB_1-kB_2\right)^{2/3}} \right\}_{\mathcal{Q}} d\tilde{\mathbf{y}}$$

If $mB_1 - kB_2 \neq 0 \rightarrow \Psi = \frac{1}{\beta_{0_1}}\eta_{\text{CRF}} M_{\text{tip}_1} M_{0_1}\chi_s + (\varphi_s - \varphi), \qquad \eta_{\text{CRF}} = \frac{mB_1 + kB_2\Omega_2/\Omega_1}{mB_1 - kB_2}$

(4c)

If $mB_1 - kB_2 = 0 \rightarrow \Psi = \frac{1}{\beta_{0_1}}\eta_{\text{CRF}} M_{\text{tip}_1} M_{0_1}\chi_s, \qquad \eta_{\text{CRF}} = 1 + \frac{\Omega_2}{\Omega_1}$

where $M_{\text{tip}_1} = \Omega_1 R_{\text{tip}_1}/c_0$ is the tip rotational Mach number of the front rotor. The parameters γ, μ, $d_{0,n}$, and $d_{1,n}$ are given by the following expressions

$$\mu = \frac{1}{2}\left[\Phi(v^+) + \Phi(v^-)\right], \qquad \gamma^3 = \frac{3}{4}\left[\Phi(v^+) - \Phi(v^-)\right]$$

$$d_{0,n} = \frac{\Gamma_n(\gamma) + \Gamma_n(-\gamma)}{2}, \qquad d_{1,n} = \frac{\Gamma_n(\gamma) - \Gamma_n(-\gamma)}{2\gamma}, \qquad \Gamma_n(\zeta) = \frac{\mathcal{A}^{(n)}\left[v(\zeta)\right]}{R^n\left[v(\zeta)\right]} \frac{dv}{d\zeta}, \qquad \frac{dv}{d\zeta} = \frac{\gamma^2 - \zeta^2}{\Phi'\left[v(\zeta)\right]}$$

(4d)

$$\Phi(\theta) = i\left(\theta + a_s\sqrt{1 - b_s\cos\theta}\right), \qquad \theta = \Omega_1\tau + \varphi_s - \varphi, \qquad b_s = \frac{2rr_s}{\chi_s^2 + r^2 + r_s^2}, \qquad \chi_s = \frac{1}{\beta_{0_1}}(x_1 - y_1)$$

$$\underbrace{a_s = \frac{M_{\text{tip}_1}}{\beta_0}\sqrt{\chi_s^2 + r^2 + r_s^2}}_{\text{for Thickness Source}}, \qquad \underbrace{a_s = \frac{1}{\beta_0}\eta_{\text{CRF}} M_{\text{tip}_1}\sqrt{\chi_s^2 + r^2 + r_s^2}}_{\text{for Loading and Quadrupole Sources}}$$

where $v^{\pm}$ are the saddle points of the phase function $\Phi(\theta)$ with $v = \theta + i\sigma$ being an extension of the real variable θ into the complex plane. The terms Ai and Ai' denote the Airy function and its derivative. The expressions inside the curly brackets in Eq. (4a - 4c) are closed form formulas for the radiation efficiencies of the thickness, loading and quadrupole sources (i.e., the integrals over τ). Note that whereas the radiation efficiency and azimuthal mode content of the thickness source depend on the parameter mB_1, those for the loading and quadrupole sources depend on the parameter $mB_1 - kB_2$. Finally, the coefficients $\mathcal{A}_{T_m}^{(n)}$, $\mathcal{A}_{\mathcal{L}_m}^{(n)}$ and $\mathcal{A}_{\mathcal{Q}_m}^{(n)}$ are given by

$$\mathcal{A}_{T_m}^{(1)} = \frac{imB_1\Omega_1}{4\pi\kappa}\left[1 + \frac{1}{\kappa}\left(g_c M_{0_i} M_{0_i} - M_{0_R}\right)\right]\rho_0 v_n$$

$$\mathcal{A}_{T_m}^{(2)} = \frac{c_0}{4\pi\kappa^3} M_{0_R}\left(\beta_{0_1}^2 + M_{0_i} M_{0_i}\right)\rho_0 v_n$$

(5a)

$$\mathcal{A}_{\mathcal{L}_{m,k}}^{(1)} = -\frac{i\left(mB_1\Omega_1 + kB_2\Omega_2\right)}{4\pi c_0\kappa^2}\hat{p}_k\left(g_c M_{0_i} - e_i\right)n_i$$

$$\mathcal{A}_{\mathcal{L}_{m,k}}^{(2)} = -\frac{1}{4\pi\kappa^3}\hat{p}_k\left(\beta_0^2 e_i + M_{0_R} M_{0_i}\right)n_i$$

(5b)

$$\mathcal{A}_{\mathcal{Q}_{m,k}}^{(1)} = -\frac{\left(mB_1\Omega_1 + kB_2\Omega_2\right)^2}{4\pi c_0^2\kappa^3}\left[e_i e_j + g_c^2 M_{0_i} M_{0_j} - g_c\left(M_{0_i} e_j + M_{0_j} e_i\right)\right]\hat{T}_{ij_k}$$

$$\mathcal{A}_{\mathcal{Q}_{m,k}}^{(2)} = \frac{i\left(mB_1\Omega_1 + kB_2\Omega_2\right)}{4\pi c_0\kappa^4}\left[\kappa^2\delta_{ij} - 3\beta_0^2 e_i e_j + \left(1 + 2g_c M_{0_R}\right)M_{0_i} M_{0_j} - \left(3M_{0_R} - \kappa\right)\left(M_{0_i} e_j + M_{0_j} e_i\right)\right]\hat{T}_{ij_k}$$

(5c)

$$\mathcal{A}_{\mathcal{Q}_{m,k}}^{(3)} = \frac{1}{4\pi\kappa^5}\left[-\beta_0^2\kappa^2\delta_{ij} + 3\beta_0^4 e_i e_j + \left(3M_{0_R}^2 - \kappa^2\right)M_{0_i} M_{0_j} + 3\beta_0^2 M_{0_R}\left(M_{0_i} e_j + M_{0_j} e_i\right)\right]\hat{T}_{ij_k}$$

where δ_{ij} is the Kronecker delta. In deriving these expression only the periodic part of the unsteady aerodynamic flowfield is considered. In other words, the aerodynamic flowfield has been assumed to have the form:

$$f(\tau) = -\left(\sum_{k=-\infty}^{\infty}\hat{p}_k e^{-ikB_2(\Omega_1+\Omega_2)} - p_0\right), \qquad \rho(\tau) = \sum_{k=-\infty}^{\infty}\hat{\rho}_k e^{-ikB_2(\Omega_1+\Omega_2)}, \qquad u_i(\tau) = \sum_{k=-\infty}^{\infty}\hat{u}_{i_k} e^{-ikB_2(\Omega_1+\Omega_2)}$$

(6a)

which reflects the fact that in a frame of reference rotating with the front rotor, the flowfield will have harmonic unsteadiness in the relative blade passing frequency $B_2(\Omega_1 + \Omega_2)$ of the aft rotor. Note that, due to its non-linear dependence on the primitive flow variables, the Reynolds stress component of the Lighthill tensor in Eq. (1) will have to be expanded and regrouped so that it can be written in terms of a single Fourier series of the form

$$T_{ij}(\tau) = \sum_{k=-\infty}^{\infty}\hat{T}_{ij_k} e^{-ikB_2(\Omega_1+\Omega_2)}$$

(6b)

Naturally, this is practical only when a finite number of Fourier terms are considered in the primitive flow variables. For example, if one limits the series in Eq. (6a) to the range $-3 \le k \le 3$, the resulting expansion and regrouping for the $k = 0$ term in the Fourier expansion of T_{12} will have the form

$$\hat{T}_{12_0} = \hat{\rho}_0 \left(\hat{u}_0 \hat{v}_0 + \hat{u}_1 \hat{v}_{-1} + \hat{u}_{-1} \hat{v}_1 + \hat{u}_2 \hat{v}_{-2} + \hat{u}_{-2} \hat{v}_2 + \hat{u}_3 \hat{v}_{-3} + \hat{u}_{-3} \hat{v}_3 \right) + \hat{\rho}_1 \left(\hat{u}_0 \hat{v}_{-1} + \hat{u}_{-1} \hat{v}_0 + \hat{u}_1 \hat{v}_{-2} + \hat{u}_{-2} \hat{v}_1 + \hat{u}_2 \hat{v}_{-3} + \hat{u}_{-3} \hat{v}_2 \right) +$$
$$\hat{\rho}_{-1} \left(\hat{u}_0 \hat{v}_1 + \hat{u}_1 \hat{v}_0 + \hat{u}_2 \hat{v}_{-1} + \hat{u}_{-1} \hat{v}_2 + \hat{u}_3 \hat{v}_{-2} + \hat{u}_{-2} \hat{v}_3 \right) + \hat{\rho}_2 \left(\hat{u}_{-1} \hat{v}_{-1} + \hat{u}_0 \hat{v}_{-2} + \hat{u}_{-2} \hat{v}_0 + \hat{u}_1 \hat{v}_{-3} + \hat{u}_{-3} \hat{v}_1 \right) +$$
$$\hat{\rho}_{-2} \left(\hat{u}_1 \hat{v}_1 + \hat{u}_0 \hat{v}_2 + \hat{u}_2 \hat{v}_0 + \hat{u}_{-1} \hat{v}_3 + \hat{u}_3 \hat{v}_{-1} \right) + \hat{\rho}_3 \left(\hat{u}_0 \hat{v}_{-3} + \hat{u}_{-3} \hat{v}_0 + \hat{u}_1 \hat{v}_{-2} + \hat{u}_{-2} \hat{v}_{-1} \right) \tag{6c}$$

with comparable expressions for the terms corresponding to $k = \pm 1, \pm 2, \pm 3$ in the Fourier expansion of T_{12} as well similar expressions for the other eight components of the Lighthill tensor.

The spatial integrations in the Eqs. (4a-4c) can be carried out using quadrature schemes in order to retain the complexity of the blade shapes and the associated flowfields. It should be noted that the spatial integrations in the FW-H equation over the rotor surface and the volume surrounding it (i.e., S and V) have been reduced to those over a single blade and the volume surrounding it (i.e., S_{B_1} and V_{B_1}). Furthermore, a length-preserving transformation has been used to transform the integrals from the stationary frame of reference to a rotating frame of reference (i.e., $\mathbf{y} \rightarrow \tilde{\mathbf{y}}$) fixed to the front rotor in order to make the integrals easier to evaluate.

The expressions for the aft rotor tone noise field are identical to those for the front rotor, but with the (B_1, Ω_1) pair interchanged with (B_2, Ω_2) pair in the Eqs. (3–6). Note that m and k indices are not interchanged. Additionally, in the aft rotor expressions, the term $(\varphi_s - \varphi)$ is replaced with $-(\varphi_s - \varphi)$ owing to the opposite sense of rotation of the aft rotor. The overall open rotor tone field is the sum of the contributions from the two rotors. These expressions have been incorporated into the NASA Glenn open rotor noise codes LINPROP and QPROP in order to predict the tone noise of contra-rotating open rotors. The original versions of these codes (developed circa 1992) were applicable only to single rotation rotors.[8] It should be noted that the LINPROP code includes the expressions for the thickness and loading noise sources and the QPROP code includes those for the quadrupole noise source.

B. Aerodynamic Simulations

For the purposes of this paper, the aerodynamic flowfields necessary for source strength specification in the LINPROP and QPROP codes were generated using the commercial CFD software package FINE[TM]/Turbo developed by NUMECA International. FINE[TM]/Turbo is a structured, multi-block, unsteady Navier-Stokes solver which can be run in the full unsteady mode as well as in the nonlinear harmonic, NLH, mode (see He[11]). In the NLH mode, the unsteady solution is obtained for a pre-selected, and finite, number of the blade passing frequency harmonic components of the time-dependent solution. All other unsteady content is ignored. The net result is a substantial reduction in the computational resource and time requirements compared with a full unsteady approach. For a well-resolved grid, an NLH simulation takes 5-6 times longer to converge than the steady state solution on the same grid. In contrast, a full unsteady simulation takes at least 100 times longer than the steady state solution to converge and requires a substantially larger grid. For that reason, in this paper, the NLH solution approach was chosen for the purpose of computing the aerodynamic response needed for input to the acoustic model. In addition, the mean flowfield and the first three harmonics of the blade-passing frequency content of the unsteady flow have been taken into account for each rotor. With this choice, all relevant acoustic tones content up to the 66th shaft order can be modeled.

In the NLH simulations generated for this work, the computational domain includes one passage for each rotor and its associated ancillary domains such as the spinner, hub, farfield, etc. as shown in Figure 3. The total mesh size for these simulations was approximately 27.1 million grid points with the
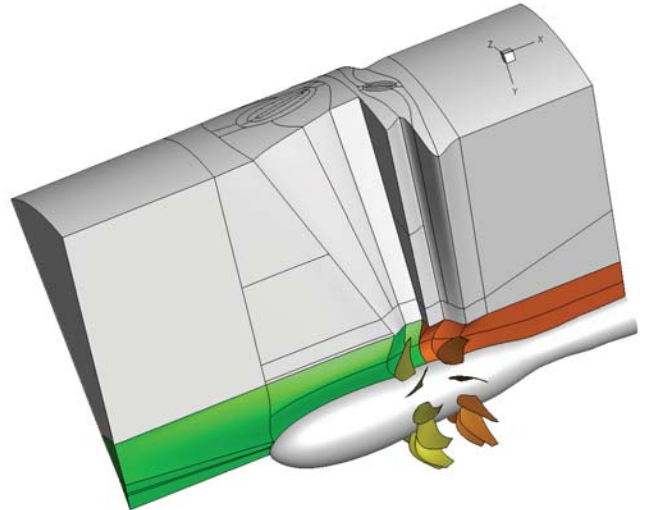
Figure 3. The computational domain and grid blocks used for nonlinear harmonic FINE[TM]/Turbo simulations used in this study. The blocks associated with each rotor are distinguished by a different color though the "farfield" blocks for both rotors are shown in gray.

7

farfield boundary set at slightly more than four tip radii away. The computations were run in parallel mode by partitioning the grid into 73 distinct blocks, which resulted a computational load balance of 98%.

A total of eight aerodynamic simulations were carried out for this study. Table 1 shows the tip speed conditions investigated which all had equal RPMs for the front and aft rotors. These tip speeds correspond to the cruise condition for this model scale blade set. It should be noted that neither the aerodynamic simulations, nor the CROR tone noise model, are restricted to the equal RPM cases, but the equal RPM represents the typical operating condition for open rotors unless there is a need for optimizing the front and aft rotor thrust or torque balance. For all of the cases studied here, the nominal blade setting angles for the front and aft rotors were, respectively, 64.4^o and 61.8^o and the "forward flight speed" was set at Mach 0.78. Each aerodynamic simulation was run at least 5,000 iterations until all monitored (mean and perturbation) residuals had been reduced by at least three orders of magnitude and were no longer changing in any meaningful way. The mean flowfield was well converged after about 1,000 iterations, but the perturbation flowfield required the additional iterations to achieve convergence. The simulations were run on a 16-core desktop computer with 192 GB of RAM though the maximum memory requirement for these simulations did not exceeded 100 GB.

Table 1. F31/A31 corrected rotor tip speeds investigated in this study.

Case	Front / Aft Rotor RPMs
1	5640 / 5640
2	6013 / 6013
3	6256 / 6256
4	6389 / 6389
5	6579 / 6579
6	6700 / 6700
7	6774 / 6774
8	6848 / 6848

Figure 4 shows a comparison of total thrust predicted by FINE^{TM}/Turbo package versus the measured thrust obtained in the NASA 8-foot x 6-foot aerodynamic wind tunnel for the cruise condition tip speeds investigated. The agreement is quite reasonable for acoustic analysis purposes with a maximum discrepancy of less than 5% at the highest tip speed and with the thrust predictions for most other tip speeds agreeing to better than 2% with the measured data. It should be noted that no tweaks were performed to adjust the blade angles, rotor tip speeds, or the flight Mach number in order to achieve a better match with the measured data. In other words, the simulations represent predictions in the true sense of the word. It should also be noted that the blade shapes at the max climb condition were used for all cruise cases considered here. Thus, small variations in the blades' hot shapes due to the changes in centrifugal force as a function of RPM difference relative to the max climb were ignored. In other words, the same shapes were used for all of the tip speeds investigated here.

In the interest of brevity, details of the aerodynamic predictions are not discussed here, but it should be noted that the results indicate that the mean and perturbation loading levels on the aft rotor are higher than those on the front rotor. The aft rotor experiences higher level of aerodynamic forcing due to the impingement of the wake and tip vortex of the front rotor, whereas the front rotor is only weakly affected by the potential field of the aft rotor. Finally, the first harmonic perturbation is roughly two orders of magnitude smaller than the mean flowfield and the second and third harmonic perturbations are smaller than the first harmonic component by approximately factors of two and four, respectively.

From the simulated aerodynamic flowfield, the blade surface harmonic pressure distribution $\hat{p}_k$ for each rotor and the harmonic components of the Lighthill tensor $\hat{T}_{ij_k}$ in the vicinity of each rotor were extracted or computed and, together with the blade geometries, were supplied as inputs to the LINPROP and QPROP codes. The codes were run for all of the cases considered here for a large number of "observer" locations that
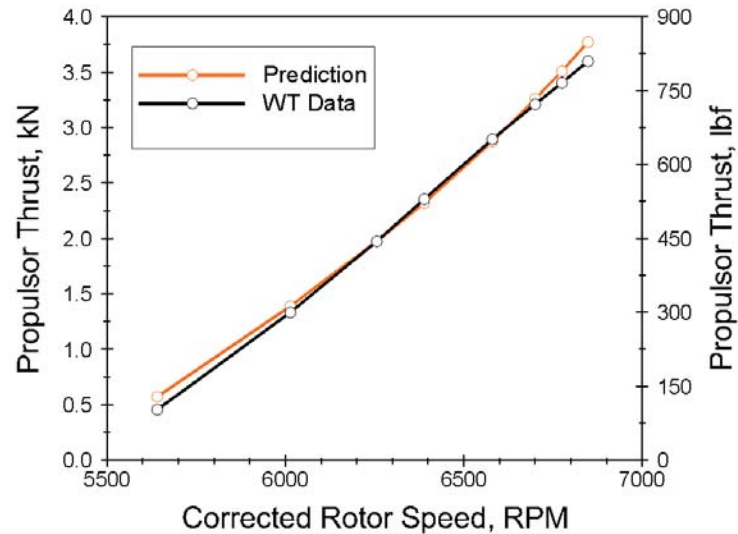
Figure 4. Comparison of predicted and measured model scale F31/A31 thrust across the speed range investigated in this study. Combined thrust by both rotors is plotted.

Figure 5. Model scale F31/A31 blade set installed in the NASA 8-foot x 6-foot high-speed wind tunnel. The plate shown suspended above the rotor has embedded Kulites that were used for nearfield acoustic measurements, which were used for assessing the acoustic predictions in this paper.
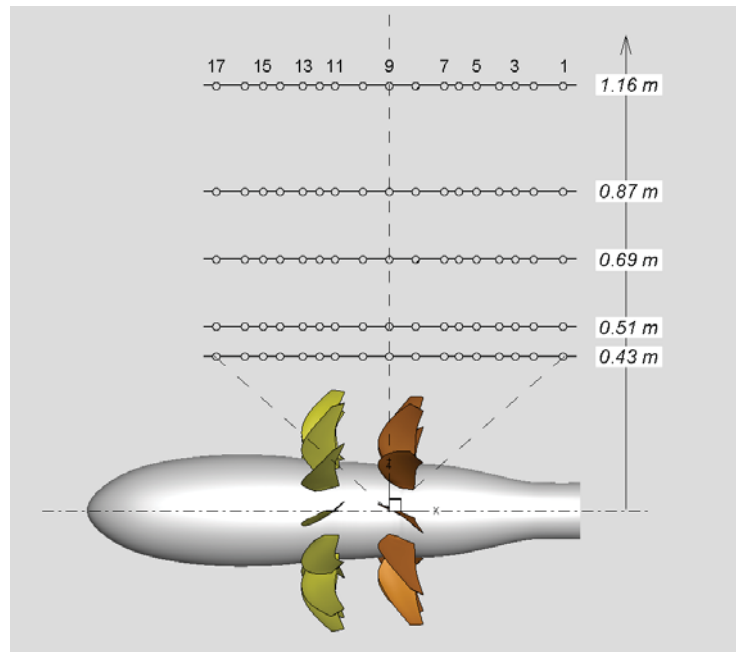
correspond to the set of acoustic pressure measurements that were acquired in the NASA 8-foot x 6-foot aerodynamic wind tunnel for the F31/A31 blade set operating at the cruise condition (See Figure 5). The experimental setup and the acoustic measurement scheme are discussed in the next section.

III. Wind Tunnel Measurements

The acoustic data used in this study were acquired at Mach 0.78 corresponding to the cruise condition for the model F31/A31 blade set. The 8x6 tunnel is not acoustically treated, nonetheless meaningful acoustic data can be acquired in the acoustic nearfield in this tunnel. Close to the source (the F31/A31 model in this case), the reflections from the untreated walls of the tunnel would be weaker than the direct radiated field from the rotors arriving at the pressure sensors especially when the measurement location is in the close proximity of the open rotor. As such nearfield measurements of acoustic field should be reasonably accurate and reliable. Such nearfield measurements could be used for assessing the impact of the open rotor noise field on the fuselage or cabin.

The acoustic measurements in the 8x6 wind tunnel were acquired using Kulite pressure sensors embedded in a steel plate suspended from the ceiling of the tunnel above the F31/A31 model as shown in Fig. 5. The plate could be lowered or raised vertically in order to investigate the dependence of the acoustic nearfield on the distance from the open rotor. The vertical positions of the plate at which Kulite measurements were acquired are shown in Figure 6. The plate was installed in the tunnel so that its centerline was parallel and in the same vertical plane as the open rotor rotational axis. Seventeen Kulites were flush mounted in the plate along its centerline with the middle Kulite located exactly above the stacking axis of the aft rotor (i.e., at $x = 0$ m in the coordinate system shown in Fig. 2) and the rest were non-uniformly, but symmetrically, distributed on either side of the stacking axis location. The axial locations of the Kulites in the coordinate system of Fig. 2 are listed in Table 2 and are graphically shown as small circles in Fig. 6. Note that the geometric angle of the each Kulite relative to the coordinate origin changes with the vertical position of the plate.

At each plate position, the data were acquired simultaneously for all 17 Kulties at a sampling rate of 200 kHz over a 15-sec time interval. Using a 2^{14} FFT stencil,


Figure 6. Sketch showing the vertical position of the acoustic plate relative to the F31/A31 rotational axis. The range of locations is from 0.43 m (16.8 inches) for the nearest plate position to 1.61 m (45.7 inches) for the farthest position. The pressure measurements were acquired at all 17 Kulites indicated by the small circles.

auto- and cross-power spectra (relative to $20\,\mu$Pa) were computed from the time series resulting in a spectral frequency bin-width of 12.2 Hz. For the purposes of this study, only the auto-spectra are considered. An example of a typical auto-spectrum is shown in Figure 7 for the highest tip speed case, namely, 6848/6848 RPM. Note that the

Table 2. Kulite axial locations.

Kulite #	Axial Location	
	Meters	**Inches**
1	0.467	18.4
2	0.389	15.3
3	0.340	13.4
4	0.295	11.6
5	0.234	9.2
6	0.188	7.4
7	0.147	5.8
8	0.071	2.8
9	0.000	0.0
10	-0.071	-2.8
11	-0.147	-5.8
12	-0.188	-7.4
13	-0.234	-9.2
14	-0.295	-11.6
15	-0.340	-13.4
16	-0.389	-15.3
17	-0.467	-18.4

principal abscissa in this figure is shown in terms of the shaft orders of the open rotor. This makes identifying the individual rotor tones and rotor-rotor interaction tones very easy. The tone levels plotted include a 6-dB correction to account for the pressure doubling at the plate surface. The dominant tones in this figure are labeled according to their origin, i.e., whether they are generated by the individual rotors or by their interactions. As was pointed out in Section II, theoretically, contra-rotating open rotor tones have frequency content dictated by the combination $mB_1\Omega_1 + kB_2\Omega_2 = m\text{BPF}_1 + k\text{BPF}_2$ where BPF_1 and BPF_2 are the blade passing frequencies of the front and aft rotors. Of course, a close examination of the spectrum in Fig. 7 reveals that not only there are even order tones present in this spectrum, but also odd order ones as well. These latter tones are not predicted by the theory since even blade counts of the two rotors (i.e., 12 and 10) can only give rise to sum and difference frequency combinations that are even ordered. The discrepancy can be explained as follows. In the theory (both aerodynamic and acoustic) the blades in each rotor disc are assumed to be identical and assumed to experience the same time history over the course of one rotor revolution but displaced spatially and temporally from that of the reference blade. In the actual hardware, the composite blades were hand-finished, which likely introduced small blade-
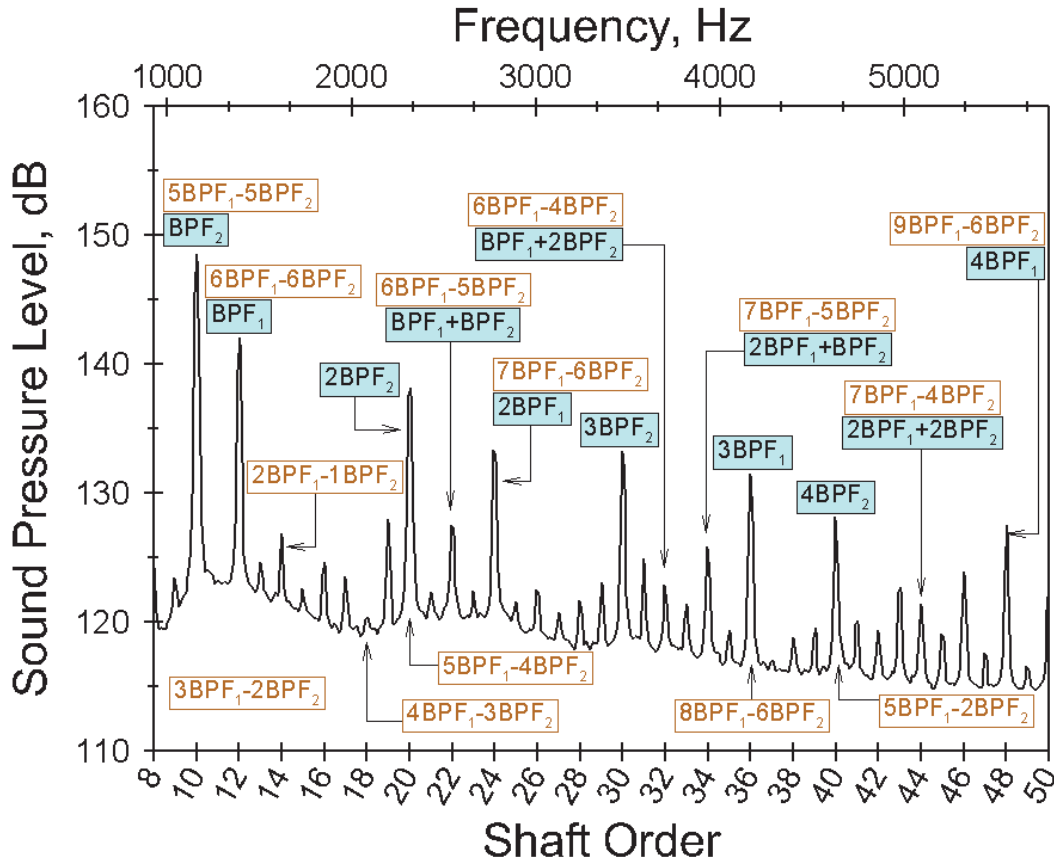
Figure 7. Sound pressure level (SPL) of the F31/A31 blade set at the corrected 6848/6848 RPM tip speed measured by Kulite #9 with the plate positioned at 1.16 m (45.7 inches) above the rotor axis. The SPL is plotted versus multiples of the open rotor shaft frequency (i.e., shaft orders). The uncorrected shaft frequency for this case is 115.7 Hz. A 6-dB correction has been applied to the measured data to compensate for the pressure doubling caused by the presence of the plate. Various tones are identified according to their origin.

to-blade geometric variations. More importantly, the installed blades showed slight blade-to-blade variations in the blade setting angles around the wheel, typically in the range of $\pm 0.25^{\circ}$. The end result of these "imperfections" is that the real blades in a rotor disc (and their associated flowfields) do not, in fact, experience exactly the same time histories and exactly the same aerodynamic levels over one period of rotor revolution. Therefore, for the actual rotors, the precise phasing assumed by the theory does not occur a consequence of which is that some of the acoustic energy is distributed amongst all shaft orders not just those singled out by the theory. Nevertheless, as can be seen from the spectrum in Fig. 7, the amount of energy leaked into these "extraneous" tones is small relative to the energy remaining in the theoretically predicted tones. As such, these real blade effects should not dramatically influence the basic aspects of the physics of the problem, which are modeled by the theory. The validity of this assertion can be assessed by the level of data-theory agreement in the next section.

IV. Assessment of Acoustic Predictions

We begin the assessment of the accuracy of the acoustic predictions by comparing the predicted and measured tone spectra for the highest tip speed condition (i.e., 6848/6848 RPM case) for the Kulite #9 with the plate at its farthest position (i.e., 1.16 m above the rotor rotational axis). The comparisons are for the same location as the measured spectrum in Fig. 7. The data-theory comparisons are shown in Figure 8 and include: the combined predicted levels of the thickness and loading tone sources computed using the LINPROP code (olive bars), the predicted levels from the quadrupole tone source computed using the QPROP code (blue bars), the predicted tone levels from the sum of the thickness, loading and quadrupole sources calculated by adding the LINPROP and QPROP predictions together (orange bars), and the measured data from the 8x6 wind tunnel (black bars). It should be noted that the measured tone levels in this figure (and all subsequent ones) include the sum of the power in the two or three frequency bins over which the tone is typically spread (see Fig. 7).

Overall, the predicted total levels (orange bars) agree well with the measured tone levels (black bars) for the harmonics of the individual rotor blade passing tones, namely, nBPF$_1$ and nBPF$_2$ with an average discrepancy of 2 dB. In fact, the agreement for the strongest tones (i.e., BPF$_1$, BPF$_2$ and 2BPF$_2$) is excellent being less than 1 dB. For the weaker tones, comprised mostly of the interaction tones, the agreement is only fair with the average difference of 5 dB, though the difference for some of the stronger tones among this group is actually around 3 dB or less. While the experimental uncertainty for the Kulite measurements has not been established, experience suggests an uncertainty band of at least ± 1dB, which makes the data-theory agreement quite reasonable given that no attempt was made to "tweak" the aerodynamic simulation in order to get a better match with the acoustic data.

A noteworthy feature of the results shown in Fig. 8 is that, whereas for the blade passing frequencies of the two rotors (i.e., BPF$_1$ and BPF$_2$) the quadrupole source does not play an important role in determining their level, for most other tones the inclusion of the quadrupole source improves the data-theory agreement considerably when compared with the LINPROP only predictions. This result indicates that quadrupole source is important and should be included for a better data-theory agreement for high-speed contra-rotating open rotors. This conclusion is in agreement with the previous studies (e.g., see Refs. 7 and 8), which suggest that quadruple source becomes important at the transonic and supersonic tip relative Mach numbers. The tip relative Mach numbers for the F31/A31 model at the highest tip speed case considered in this study are slightly supersonic at 1.04 and 1.03, respectively. The corresponding tip relative Mach numbers for the lowest tip speed case examined here are 0.97 and 0.95, which are in the transonic regime, and hence similar arguments apply.

Another interesting aspect of the predicted results is the relative contributions of the thickness and loading sources to the tone levels of the individual rotors. Table 3 shows the source breakdown as computed by the LINPROP code at the highest tip speed condition for the Kulite #9 when the plate was at 1.16 m above the rotor rotational axis. Whereas for the front rotor, the thickness noise level is comparable or higher than the loading noise level, for the aft rotor the loading noise level is always considerably higher than the thickness noise level. This pattern is fairly consistent across the tip speeds, plate positions, and Kulite locations investigated in this paper. The relative difference in the front and aft rotors loading noise level is principally caused by the higher blade loading levels experienced by the aft rotor as a result of the impingement of the front rotor wake and tip vortex. It should be noted that the relative difference between the thickness noise levels for the front and aft rotors seen in Table 3 varies considerably as a function of the tip speed, plate position and Kulite location and does not represent a consistent pattern throughout.

Next, the predicted and measured levels for a few representative tones as a function of the plate location are plotted in Figure 9 for the Kulite #9. The predicted levels in this figure (and all subsequent ones) include the sum of the contributions from all three sources of open rotor noise, namely, thickness + loading + quadrupole. The comparisons are shown for the blade passing frequencies of the front and aft rotors, BPF$_1$ and BPF$_2$, which are the

dominant tones at all operating conditions investigated in this paper, and the two representative interaction tones, BPF_1+BPF_2 and $2BPF_1+2BPF_2$, which are considerably weaker. The auxiliary abscissa shows the vertical plate
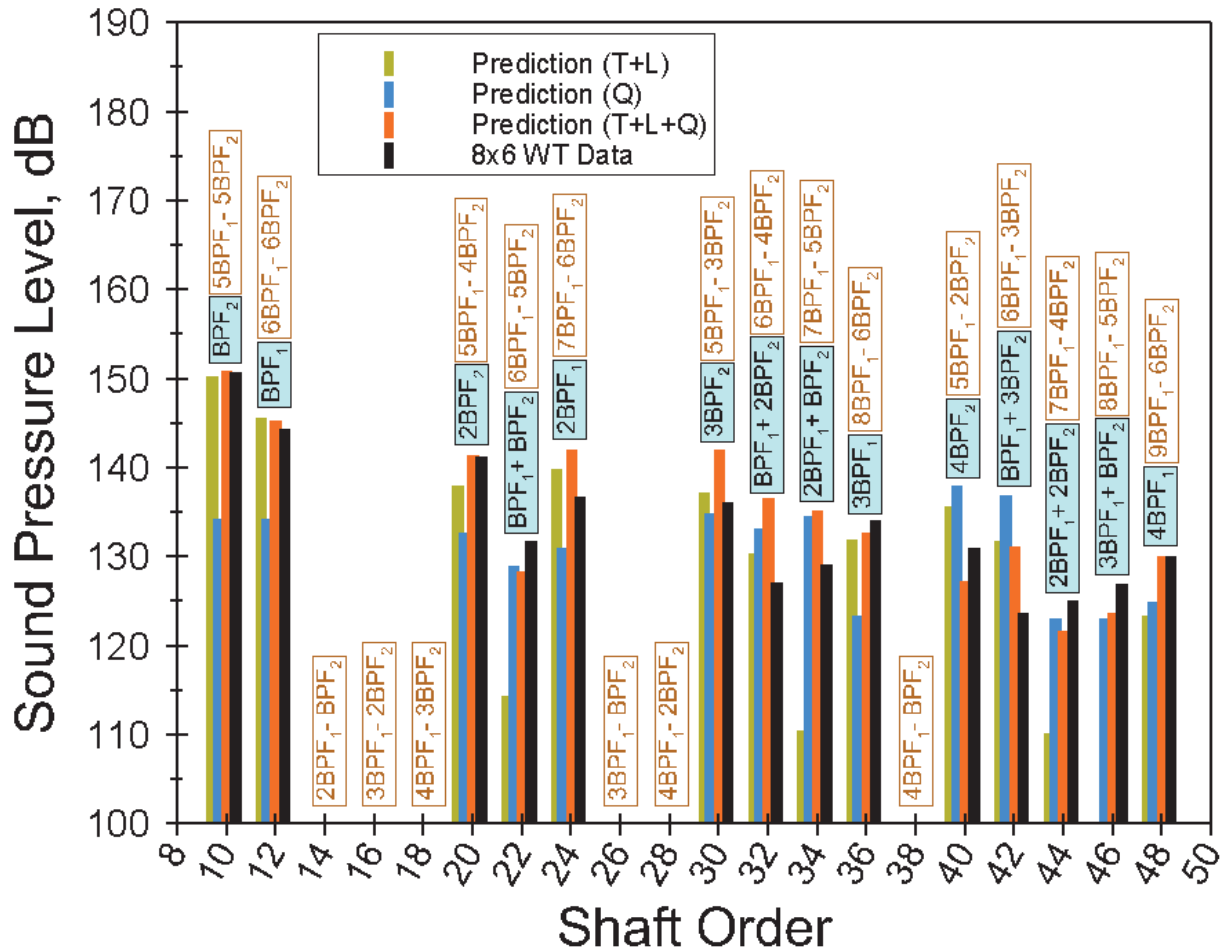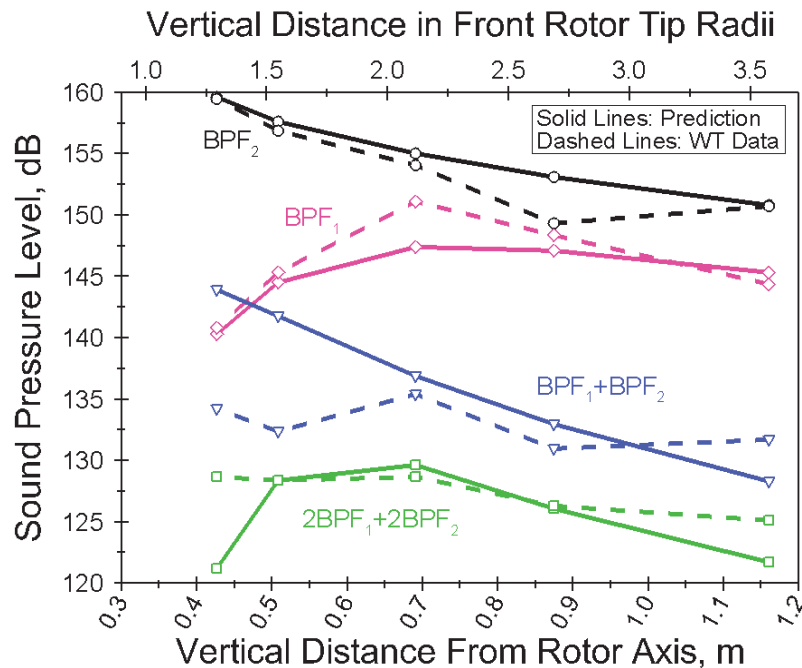

Figure 8. Comparison of predicted and measured tone SPL for F31/A31 blade set at the 6848/6848 RPM condition for the Kulite #9 with the plate positioned 1.16m (45.7 inches) above the rotor rotational axis. The predicted levels include the sum of the thickness and loading noise levels computed using the LINPROP code (olive bars), the quadrupole noise level computed using the QPROP code (blue bars), the predicted total, i.e., thickness + loading + quadrupole noise level (orange bars), and the measured levels in the wind tunnel (black bars).

Table 3. Predicted contributions of thickness and loading noise at the 6848/6848 RPM condition. Levels are for the Kulite #9 with the plate positioned 1.16 m above the rotor axis.

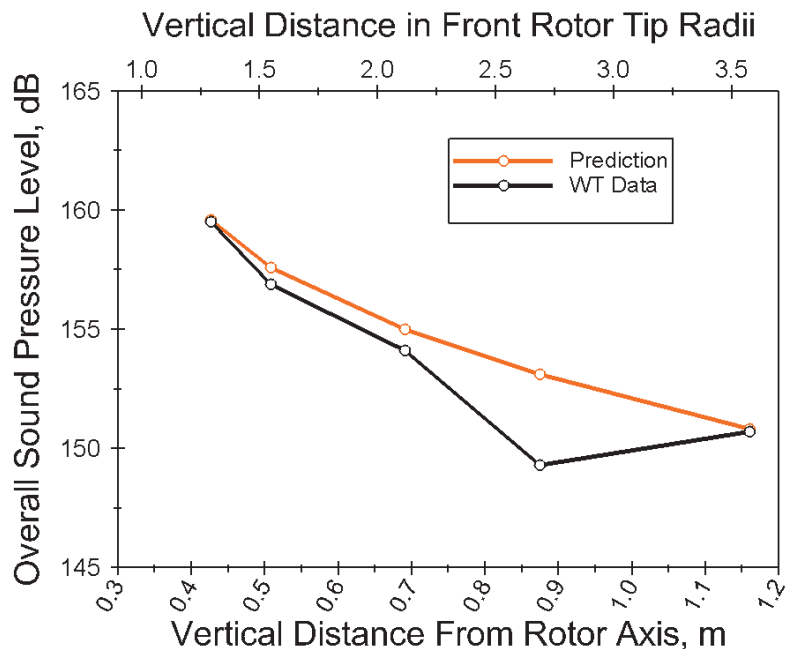| Front Rotor				Aft Rotor			
Tone (S.O.)	Thickness	Loading	Total (LINPROP)	Tone (S.O.)	Thickness	Loading	Total (LINPROP)
BPF_1 (12)	141.4	139.2	145.6	BPF_2 (10)	128.2	150.3	150.3
$2BPF_1$ (24)	136.8	130.0	139.8	$2BPF_2$ (20)	123.2	138.8	138.0
$3BPF_1$ (36)	123.6	128.1	131.9	$3BPF_2$ (30)	102.2	137.1	137.2
$4BPF_1$ (48)	127.9	125.9	123.4	$4BPF_2$ (40)	117.7	135.6	135.6
$5BPF_1$ (50)	126.9	122.1	123.2	$5BPF_2$ (50)	105.9	124.9	125.6

Figure 9. Comparison of predicted and measured tone SPL for F31/A31 blade set at the 6848/6848 RPM condition for the Kulite #9 as a function of the plate position. The predicted levels include the sum of thickness, loading and quadrupole noise sources calculated by combining the LINPROP and QPROP predictions. Predicted levels are shown as solid lines and the corresponding measured levels as dashed lines.

distance from the rotor rotational axis in the units of the front rotor tip radius (which is 0.327 m) to provide a perspective on the proximity of the plate to the open rotor. Predicted levels are shown as solid lines and the corresponding measured levels as dashed lines. The data-theory agreement is remarkably good for the BPF_1 and BPF_2 tones showing generally excellent agreement in both absolute levels and trends. Data-theory discrepancy for these tones is less than 1 dB everywhere except at one plate position for each tone where it is around 3 dB. The data-theory agreement is only fair for the BPF_1+BPF_2 and $2BPF_1+2BPF_2$ tones with an average error of about 3 dB though in most cases the error is actually less than that. These favorable comparisons show that the dominant acoustic field is well predicted by the theory.

In order to examine the data-theory agreement further, in Figure 10, the predicted and measured tone overall sound pressure level (OASPL) for all of the predicted tones are plotted as a function of the plate position for the Kulite #9. Recall that, since only the mean and the first three harmonics of the unsteady flowfield have been modeled in the aerodynamic simulations, only acoustic tones up to the first 66th shaft orders can be computed. An examination of the measured data indicates that tones beyond the 50th shaft order are much weaker and do not contribute substantially to the overall acoustic field. Not surprisingly, in view of the dominance of the two blade passing tones (i.e., BPF_1 and BPF_2), the predicted and measured OASPL agreement is quite good everywhere with an average error of less than 1 dB except at one plate position where it is around 5 dB. The source of this discrepancy is not clear, thought the predicted levels show more consistency as a function of the plate distance than do the measured levels, which show a significant

Figure 10. Comparison of predicted and measured tone OASPL for F31/A31 blade set at the 6848/6848 RPM condition for the Kulite #9 as a function of the plate position.

13

American Institute of Aeronautics and Astronautics

deviation from the overall trend at the 0.87 m (34.4 inches) plate position.

Next, we examine the trend with the tip speed by plotting the behavior of the tone OASPL as a function of the rotor tip speed for the nearest and farthest plate positions for the Kulite #9. The results are shown in Figure 11. Measurements were carried out at all tip speed conditions for the farthest plate position (i.e., 1.16 m) only. At all other plate positions, data at the 6774/6774 RPM and 6700/6700 RPM conditions were not acquired. As a result, the measured data line for the nearest position (i.e., the black line) is not continuous. There is generally very good agreement between the predicted and measured tone OASPL for the nearest plate position with one exception. The predicted OASPL at the lowest speed (5640/5640 RPM)
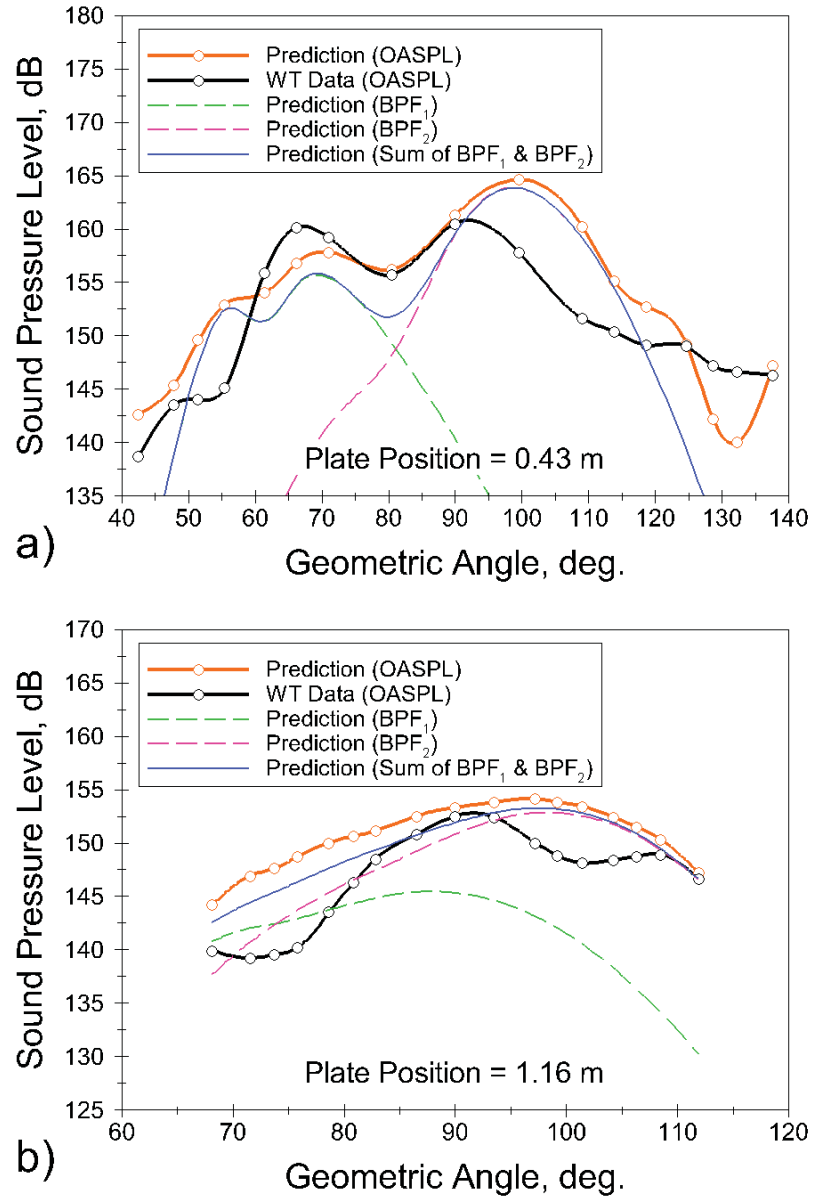

Figure 11.   Comparisons of predicted and measured tone OASPL for F31/A31 blade set for the Kulite #9 as a function of the rotor tip speed. Predicted levels for the nearest and farthest plate positions are shown.

shows a significant departure from the data (roughly 7 dB). The source of this discrepancy is not entirely clear though an examination of the loading distribution on the aft rotor reveals a noticeable difference between it and the corresponding distribution at the next higher speed (6013/6013 RPM). In addition, a comparison of the predicted and measured thrusts produced by the aft rotor shows that the predicted thrust is more than twice that of the measured one. The aft rotor thrust comparisons at higher speeds show much smaller differences between the predictions and measurements suggesting that the behavior of the aft rotor is not well captured by the simulation at the lowest speed. Furthermore, it should be noted that the thrust produced by the aft rotor at the 5640/5640 tip speed condition is very low (i.e., 0.071 kN or 16.0 lbf) indicating that the aft rotor is approaching the windmill condition making loading prediction somewhat more difficult and the predicted results suspect. As a result, the line connecting the predicted OASPLs is drawn as dashed to this last point. As for the data-theory agreement for the farthest plate position, it is generally fair with a maximum difference of 5 dB at the 6013/6013 RPM condition though at most speeds the error is significantly smaller.

Finally, in Figure 12, the variations of predicted and measured tone OASPL with the Kulite locations are shown for the nearest plate position (a) and farthest plate position (b) at the highest tip speed condition (i.e., 6848/6848 RPM). The abscissa in these figure is given in terms of the geometric angles of the Kulites, which for the nearest plate position cover the range of approximately 42° to 138°, and for the farthest plate position the range of approximately 68° to 112°. This figure effectively shows the sideline nearfield directivity of the tone OASPL as a function of distance from the open rotor. While the magnitude of OASPL is not consistently well predicted as a function of the geometric angle, the basic trends are in good agreement with the measured data. For example, for the nearest plate position, the prediction exhibits the double peak feature observed in the test data and mimics fairly closely the behavior of the sideline directivity. These peaks reflect the fact that, close to the open rotor, the tone OASPL directivity is significantly influenced by the directivities of the blade passing frequency tones of the front and aft rotors (i.e., BPF_1 and BPF_2) whose directivities peak near their respective planes of rotation. To illustrate the point graphically, the predicted sideline directivities of these two tones (dashed green and pink lines) and that of their sum (solid blue line) are also plotted for comparison. For this plate position, the plane of rotation of the front rotor is located at 65° and that for the aft rotor is located at 90°. It should be noted that the predicted sideline directivity for the BPF_1 tone itself exhibits two peaks. The one round 55° is due to the thickness source and the other near 65° is due to the loading source. Since for the front rotor thickness noise is comparable in level to the loading noise, both peaks are evident in the BPF_1 directivity. In contrast, the directivity of the BPF_2 tone is entirely dominated by the loading noise, hence only a single peak is evident for this tone near 90°. Of course, the exact location where a given tone peaks as measured on the plate depends on a number of factors including the refraction of sound waves passing through the plate boundary layer. The theoretical model does not account for the boundary
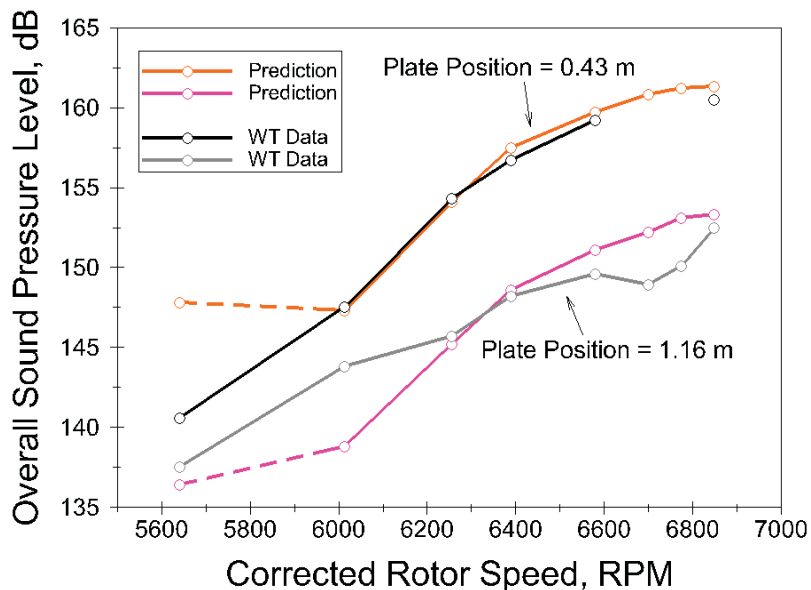
14

layer refraction, since it ignores the presence of the plate.

Farther out, it is expected that the peaks of the two tones should merge and become less distinct as the observer distance from open rotor increases owing to the dominance of the aft rotor field since the strongest tone is always the aft rotor blade passing tone (i.e., BPF_2) for the cases investigated here. The predictions are in fact consistent with this expectation. However, the behavior of the measured data is less clear for this case. There are two possible causes (among others ones) for the difference, boundary layer refraction effect and plate edge effect. For the Kulite #9 (i.e., the 90° position) and its immediate neighbors, both of these effects should be relatively small, because (1) the incident acoustic waves are falling essentially perpendicularly on the plate thus minimizing the refraction effect, and (2) these Kulites are farthest from both the upstream and downstream plate edges and hence are weakly influenced by them.[‡] As a result, the data-theory comparisons are consistently very good for the broadside Kulite locations.

However, for the Kulites near the upstream and downstream edges of the plate, the edge effect become more important and should be taken into account. Furthermore, the boundary layer refraction effect becomes more pronounced for waves falling at oblique angles on the plate, which is the case for the Kulites on the fringes. Finally, there is another complicating factor that must be taken into account when the plate is at its farthest position. At that position, the plate is retracted

a)

b)

Figure 12. **Sideline directivities of the tone OASPL for the F31/A31 blade set at the 6848/6848 RPM condition for the nearest plate position (a) and the farthest plate position (b). Predicted sideline directivities of the BPF_1 and BPF_2 tones and as well as the sideline directivity of their sum are also plotted for comparison. Note the change in the angular range from the nearest to the farthest plate positions. Both predicted and measured levels in this figure have been splined to better convey the sideline variations.**

close to the tunnel celling and is likely immersed in the tunnel boundary layer. The 8x6 tunnel boundary layer at subsonic speeds (e.g., Mach 0.78) was measured to be roughly 0.15 m (6 inches) at the test section,[12] which could substantially affect the measurements at that plate position for Kulites that are far away from the 90° location. These effects will have to be studied further for a conclusive assessment of their impact on the acoustic measurements in the 8x6 tunnel.

[‡] Note that all Kulites are located the same distance from the plate's side edges.

V. Conclusion

In this paper a fairly detailed assessment of the utility of a NASA analytical model of contra-rotating open rotor tone noise was carried out. The model is based on an asymptotic version of the Ffowcs Williams and Hawkings equation, which allows for the preservation of the geometric complexity of the rotors and their flowfield while providing accurate analytic approximations for the constituent tone content of the contra-rotating open rotor for all observer locations and tip speed conditions. High-fidelity aerodynamic simulations were used to generate the blade loading and flowfield distributions that were needed as inputs to run the acoustic model. A sizable matrix of cases involving eight rotor tip speeds corresponding to the cruise condition and a total of 85 "observer" locations were investigated to assess the ability of the CROR noise model to predict the tone spectra of a model scale contra-rotating open rotor for which substantial aerodynamic and acoustic data had been acquired in wind tunnel tests at NASA. The predicted tone spectral levels and trends show good agreement with the measured data over the range of operating conditions and observer locations examined. This is especially true for the dominant CROR tones and overall sound pressure level of tone as a function of tip speed for the broadside positions. The results also indicate that, whereas the individual rotor tones are well predicted by the combination of the thickness and loading sources, for the CROR interaction tones it is essential that the quadrupole source is also included in the analysis.

Acknowledgments

References

[1]Stephens, D. B., "Nearfield Unsteady Pressures at Cruise Mach Numbers for a Model Scale Counter-Rotation Open Rotor," *18th AIAA/CEAS Aeroacoustics Conference*, Colorado Springs, CO, 2012, Paper No. AIAA-2012-2264 and NASA/TM–2012-217672, 2012.

[2]Ffowcs Williams, J .E. and Hawkings, D. L., "Sound Generation by Turbulence and Surfaces in Arbitrary Motion," *Phil. Trans. Roy. Soc*., A264, 1969, pp. 321-342.

[3]Goldstein, M.E., *Aeroacoustics*, McGraw-Hill, New York, 1976, Chap. 4, pp.189-192.

[4]Farassat, F., Dunn, M. H., Tinetti, A. F., and Nark, D. M., "Open Rotor Noise Prediction Methods at NASA Langley – A Technology Review," *15th AIAA/CEAS Aeroacoustics Conference*, Miami, Florida, Paper No. AIAA-2009-3133, 2009.

[5]Hanson, D. B., "Noise of Counter-Rotation Propellers," *J. of Aircraft*, Vol. 22, No. 7, 1985, pp. 609-617.

[6]Parry, A. B., "Theoretical Prediction of Counter-Rotating Propeller Noise," Ph.D. Thesis, Dept. of Applied Mathematics, University of Leeds, U.K., 1988.

[7]Ffowcs Williams, J .E. and Hawkings, D. L., "Theory Relating to the Noise of Rotating Machinery," *J. Sound Vib*., 10(1), 1969, pp. 10-21.

[8]Envia, E., "Asymptotic Theory of Supersonic Propeller Noise," *AIAA Journal*, Vol. 32, No. 2, 1994, pp. 239-246.

[9]Envia, E., "Aeroacoustic Analysis of a High Speed Open Rotor," *International Journal of Aeroacoustics*, (submitted for publication).

[10]Crighton, D.G. and Parry, A. B. "Higher Approximations in the Asymptotic Theory of Propeller Noise," *AIAA Journal*, Vol. 30, No. 1, 1992, pp. 23-28.

[11]He, L. and Ning, W., "Efficient Approach for Analysis of Unsteady Viscous Flows in Turbomachines," *AIAA Journal*, Vol. 36, No. 11, 1998, pp. 2005-2011.

[12]Arrington, E. A., "Calibration of the NASA Glenn 8- by 6-Foot Supersonic Wind Tunnel (1996 and 1997 Tests)," NASA/CR–2012-217270, 2012.